PCCP

Accepted Manuscript

This is an *Accepted Manuscript*, which has been through the Royal Society of Chemistry peer review process and has been accepted for publication.

Accepted Manuscripts are published online shortly after acceptance, before technical editing, formatting and proof reading. Using this free service, authors can make their results available to the community, in citable form, before we publish the edited article. We will replace this *Accepted Manuscript* with the edited and formatted *Advance Article* as soon as it is available.

You can find more information about *Accepted Manuscripts* in the Information for Authors.

Please note that technical editing may introduce minor changes to the text and/or graphics, which may alter content. The journal's standard Terms & Conditions and the Ethical guidelines still apply. In no event shall the Royal Society of Chemistry be held responsible for any errors or omissions in this *Accepted Manuscript* or any consequences arising from the use of any information it contains.

Au-Rh and Au-Pd nanocatalysts supported on rutile titania nanorods: structure and chemical stability

Zere Konuspayeva,[1] Pavel Afanasiev,[1] Thanh-Son Nguyen,[1] Luca Di Felice,[1] Franck Morfin,[1] Nhat-Tai Nguyen,[2] Jaysen Nelayah,[2] Christian Ricolleau,[2] Ziyou Li,[3] Jun Yuan,[4] Gilles Berhault,[1] Laurent Piccolo[1,*]

[1] *Institut de recherches sur la catalyse et l'environnement de Lyon (IRCELYON), UMR 5256 CNRS & Université Claude Bernard - Lyon 1, 2 avenue Albert Einstein, 69626 Villeurbanne, France.*

[2] *Laboratoire Matériaux et Phénomènes Quantiques (MPQ), UMR 7162 CNRS & Université Paris-Diderot, Bâtiment Condorcet, 4 rue Elsa Morante, 75205 Paris Cedex 13, France.*

[3] *Nanoscale Physics Research Laboratory (NPRL), School of Physics and Astronomy, University of Birmingham, Edgbaston, Birmingham B15 2TT, UK.*

[4] *Department of Physics, University of York, Heslington, York, YO10 5DD, UK*

* Corresponding author. E-mail: laurent.piccolo@ircelyon.univ-lyon1.fr

Abstract

Au, Rh, Pd, Au-Rh and Au-Pd nanoparticles (NPs) were synthesized by colloidal chemical reduction and immobilized on hydrothermally-prepared rutile titania nanorods. The catalysts were characterized by aberration-corrected TEM/STEM, XPS, and FTIR, and were evaluated in the hydrogenation of tetralin in the presence of H_2S. Oxidizing and reducing thermal treatments were employed to remove the polyvinyl alcohol (PVA) surfactant. Reduction in H_2 at 350 °C was found efficient for removing the PVA while preserving the size (3 nm), shape and bimetallic nature of the NPs. While Au-Pd NPs are alloyed at the atomic scale, Au-Rh NPs contain randomly distributed single-phase domains. Calcination-reduction of Au-Rh NPs mostly leads to separated Au and Rh NPs, while pre-reduction generates a well-defined segregated structure with Rh located at the interface between Au and TiO_2 and possibly present around the NPs as a thin overlayer. Both the titania support and gold increase the resistance of Rh and Pd to surface oxidation. Furthermore, although detrimental to tetralin hydrogenation initial activity, gold stabilizes the NPs against surface sulfidation in the presence of 50 ppm H_2S, leading to increased catalytic performances of the Au-Rh and Au-Pd systems as compared to their Rh and Pd counterparts.

1. Introduction

Nanoalloys are currently the subject of renewed interest due to the recent progress in atomic-scale characterization techniques, such as aberration-corrected transmission electron microscopy, together with a variety of applications of such systems to industrially-important catalytic reactions.[1,2] This progress has favored the development of new nanoalloy synthesis and structural modeling methods. In heterogeneous catalysis, a large fraction of reactions are catalyzed by metals, and the catalytic performances (activity, selectivity, stability) can often be improved by alloying. Traditionally categorized as either geometric or electronic effects, the catalytic synergies provided by alloying originate from a combination of factors, such as in strain effects.

Catalytic hydrogenation of aromatic hydrocarbons, for which palladium and rhodium are among the most efficient metals, form an important class of reactions. They are used, *e.g.*, in petroleum refining to increase the combustion efficiency of fuels and reduce carcinogenic microparticle emissions.[3] In such applications, after deep hydrodesulfurization, the fuels still contain ppm amounts of sulfur, mostly in the form of H_2S. However, in spite of the nobleness of platinum-group metals, these materials readily react with S-containing species and strongly bond atomic sulfur, which possibly leads to metal sulfidation and irreversible poisoning.[4] Hence, the development of S-resistant hydrogenation catalysts is highly desirable. This goal can be achieved by using acidic supports, such as aluminosilicates, which induce electron transfers and thereby weaken the sulfur-metal bond.[5] Another approach consists in "nanoalloying" platinum-group metals with less reactive ones, such as gold, with the aim of increasing the catalyst stability.[2]

In this work, our first objective was to synthesize well-defined Au-Rh/TiO_2 catalysts using a facile preparation method similar to the one widely employed for Au-Pd nanoparticles, namely the colloidal synthesis. While Au-Pd is one of the most studied bimetallic systems due to its promising applications in catalysis,[6–17] Au-Rh has been only scarcely investigated. From bulk thermodynamics, the Au-Pd and Au-Rh systems exhibit opposite behaviors. Au and Pd are fully miscible, as shown by the bulk phase diagram.[18] In contrast, Au and Rh have a positive mixing enthalpy (ΔH_{mix}^{Au-Rh} = 7 kJ/mol vs ΔH_{mix}^{Au-Pd} = -8 kJ/mol), and a large difference in cohesion energies (E_{coh}^{Rh} - E_{coh}^{Au} = 1.94 eV >> E_{coh}^{Pd} - E_{coh}^{Au} = 0.08 eV) and surface energies (E_{surf}^{Rh} - E_{surf}^{Au} = 1.2 J/m^2 >> E_{surf}^{Pd} − E_{surf}^{Au} = 0.6 J/m^2). They also present a larger difference in lattice constants (a_{Au}-a_{Rh} = 0.28 Å > a_{Au}-a_{Pd} = 0.19 Å). [19,20] As this combination of parameters drives the trends to alloying/demixing and surface segregation,[21] it leads to a broad miscibility gap in the bulk Au-Rh phase diagram.[22] Consequently, as compared to that of Au-Pd nanoalloys, the case of Au-Rh is less favorable to alloying and the structure of Au-Rh nanoparticles is likely to depend much more strongly on the preparation conditions.

Kiss, Óvári and coworkers published the largest body of work on this system.[23–28] The authors synthesized Au-Rh particles or thin films supported on TiO_2 substrates of various forms (commercial powder, nanowires, nanotubes, and TiO_2(110) single-crystal). They used either chemical impregnation or physical vapor deposition, and a number of surface analysis techniques. It was shown that Au has a strong tendency to cover the Rh surface, and that Au inhibits the encapsulation of Rh by TiO_x layers at high temperature. Recently, Chantry *et al.* investigated the growth of Pd and Rh on Au nanorods using aberration-corrected transmission electron microscopy techniques. They showed that a randomly mixed alloy layer (4-5 atomic layers thick) forms between Au and Rh, in contrast to the sharp interface formed between the Au substrate and the Pd overlayer.[29–31] This

observation could appear contradictory with thermodynamic data but it actually shows the importance of kinetics in governing the structure of nanoalloys.[30] Consistently, using colloidal methods and small materials amounts, Schaak and coworkers successfully synthesized alloy nanoparticles of various systems, including Au-Rh.[32] Finally, García *et al*. used microwave irradiation to synthesize Ag-Rh and Au-Rh nanoparticles (NPs) capped with poly(vinylpyrrolidone) and further deposited on amorphous silica.[33,34] Catalytic testing in cyclohexene hydrogenation at ambient temperature and pressure showed some activity enhancements for the bimetallic catalysts with respect to their monometallic counterparts.

In this paper, we present an investigation of the synthesis, structural characterization, and catalytic evaluation of Au-Pd and Au-Rh NPs supported on rutile titania nanorods. The latter are used as an ideally shaped substrate for electron microscopy imaging. We focus on the system- and pretreatment-dependent chemical structure of the NPs as well as on their chemical reactivity toward oxygen and sulfur. In particular, the catalysts were tested in high-pressure hydrogenation of tetralin in the presence of traces of H_2S in order to assess the effect of Au addition on Pd and Rh thioresistance. The two bimetallic systems were compared to each other and to the monometallic systems with the aim of understanding the impact of the NP structure on their chemical stability.

2. Experimental

2.1. Preparation methods

TiO_2 rutile nanorods were prepared using a simplified procedure based on a hydrothermal method reported by Li and Afanasiev.[35] 10 g of commercial Degussa P25 TiO_2 (50 m^2/g) and 100 mL of 15 wt% H_2SO_4 solution were mixed in a Teflon reactor and placed in a sealed autoclave kept at 200 °C for 15 days. The obtained solid was washed several times with 0.1M NH_4NO_3 to remove adsorbed sulfate, then washed with distilled water, dried at 100 °C overnight, and calcined at 350 °C in air for 2 h.

Au-Pd and Au-Rh NPs, along with their monometallic counterparts, were prepared by a colloidal chemical (co)reduction route adapted from Toshima, Prati, Hutchings, and coworkers.[6–10] The metal precursors were $HAuCl_4.3H_2O$ (Strem Chemicals, 99.9%, 49 wt% Au), $RhCl_3.nH_2O$ (Sigma-Aldrich, 99.9%, 38-40 wt% Rh), and Na_2PdCl_4 (Sigma-Aldrich, 98%). In a first step, a 200 mL aqueous solution containing the two metallic precursors was prepared by adding the amounts of precursors necessary for reaching a total metal loading of 3 wt%. An $Au_{50}Pd_{50}$ composition as well as different Au-Rh compositions were envisaged. Next, a 1 wt% aqueous solution of a stabilizing agent, polyvinyl alcohol (PVA, Mw = 10,000) was added to the preceding solution while keeping always a mass ratio $m_{PVA}/m_{(Au+M)}$ of 1.2. A solution of 0.1 M $NaBH_4$, freshly prepared and kept at 0°C before use, was then dropped under stirring to the metallic precursors solution with a molar ratio $n_{NaBH4}/n_{(Au+M)}$ of 5. Note that the use of tetrabutylammonium bromide (TBAB) instead of $NaBH_4$ led to NP size inhomogeneity. The excess of reducing agent was necessary to ensure a complete reduction of the two metals. Immediately after $NaBH_4$ addition, the color of the solution changed from yellowish orange to black, indicating the reduction of Au^{3+} and $Rh^{3+}(Pd^{2+})$ ions into Au^0 and $Rh^0(Pd^0)$. Stirring was then maintained for 30 min to allow the complete decomposition of the remaining $NaBH_4$ excess. This stirring time, corresponding to NP nucleation and growth, had to be less than 1 h in the particular case of Au-Rh, since the corresponding colloids tend to agglomerate and precipitate, as observed by

dynamic light scattering.[36] The solution was then acidified to pH 3.5 by addition of HCl 0.01 M in order to favor the sol immobilization onto the TiO_2 support. HCl was employed instead of frequently used H_2SO_4 as support acidifier, since the sulfur of H_2SO_4 was seen to deactivate the metal catalysts.[37] The amount of support necessary for reaching the final metal loading was then added and stirring was kept for 3 h. Finally, the material was filtrated, washed with hot distilled water (70 °C) several times, and dried at 100 °C overnight. The final washing of the catalysts with hot water enabled the removal of residual chloride.[38]

Ex situ treatments were applied using a dedicated bench in order to remove the PVA from the metal NP surface. These oxidizing (calcination) or reducing treatments were performed by heating the samples to 350 °C (10 °C/min, 3 h plateau) in air flow or hydrogen flow (5 mL/min, 1 atm), respectively. For FTIR and XPS characterization, the treatments could be applied *in situ* at the same temperature (see next section). Before the catalytic tests, the as-prepared ("fresh") catalysts were reduced in the reactor under pure hydrogen flow (90 mL/min) at 350 °C for 3 h.

2.2. Characterization methods

The metal weights were determined by inductively coupled plasma - optical emission spectroscopy (ICP-OES, Activa instrument from Horiba Jobin Yvon). In order to dissolve them completely, the samples were treated with a mixture of H_2SO_4, aqua regia and HF at 250-300 °C.

Routine transmission electron microscopy (TEM) experiments were performed with a JEM 2010 microscope (LaB_6 filament, 200 kV operating voltage), while advanced TEM characterization results were acquired using JEM-ARM 200F equipped with a cold-field emission gun and an image aberration corrector.[39] In the present work, the microscope was operated at an accelerating voltage of 80 kV to limit radiation damage of the NPs. In addition, scanning transmission electron microscopy (STEM) observations were conducted using a JEM-2100F (FEG, 200 kV) equipped with a probe aberration corrector and a high-angle annular dark field (HAADF) detector. All three microscopes included energy dispersive X-ray (EDX) spectroscopy systems. For TEM observations, the samples were crushed in ethanol and the solution was ultrasonically stirred before dropping on a holey carbon-covered copper TEM grid, followed by drying. For STEM investigation, the samples were crushed in air using glass slides and the particles were drop casted on TEM grids.

Transmission infrared spectroscopy of adsorbed CO (CO-FTIR) was carried out using a Thermo Nicolet 6700 spectrometer (DTGS detector) combined with a new custom-made glass cell and a gas/vacuum handling system. The cell allows for *in situ* treatment (gas flow, 1 atm, RT-500 °C) of the samples, which can be moved vertically between the (upper) treatment and (bottom) analysis positions with a magnetic transfer device. The cell can be evacuated down to *ca.* 10^{-5} Pa using a turbomolecular pump, and its bottom part can be cooled down to -196 °C (*ca.* -150 °C at the sample level) thanks to an included Pyrex Dewar system filled with liquid nitrogen (LN_2). CO (Air Liquide, purity 99.997%) can be dosed gradually and automatically using a stainless steel buffer and electro-valves. The samples were prepared in the form of self-supported pellets (13 mm diameter, *ca.* 500 μm thickness, *ca.* 20 mg weight, 2.5 tons mechanical pressure). The pellets were pretreated at 350 °C (5 °C/min from RT, 1 h plateau) in H_2 flow or 20% O_2/He flow (50 mL/min) when needed, and they were outgassed at 350 °C for 1 h under vacuum. Then, the pellets were placed in analysis position and cooled down. A

reference spectrum was recorded for the clean sample. Afterwards, cumulative dosing of CO (1 μmol per dose) and subsequent spectrum acquisition were performed until the moment when saturation coverage of CO was observed in the spectra. The spectra were recorded with 128 scans and 4 cm^{-1} resolution in the 4000-900 cm^{-1} range.

The XPS analyses were carried out using an Axis Ultra DLD spectrometer from Kratos Analytical including a monochromatized Al Kα source (1486.6 eV). The analyzer was operated at 160 eV pass energy for acquisition of survey scans and at 40 eV pass energy for acquisition of high-resolution spectra. All peaks were calibrated using the Ti $2p^{3/2}$ core level as the spectral reference, which was fixed at 458.8 eV. The instrument was equipped with an *in situ* high-temperature quartz reaction cell, which allowed us to pretreat the samples by heating them at 350 °C for 3 h under H_2 flow or O_2 flow (50 mL min^{-1}, 1 atm).

2.3. Catalytic testing method

High-pressure gas-phase tetralin hydrogenation tests were performed in a flow fixed bed reactor almost identical to an apparatus described in details elsewhere.[5] The reactor itself was a stainless steel U-shape tube (4 mm internal diameter). Tetralin (Sigma-Aldrich, 99%) and hydrogen (Air Liquide, 99.999%) partial pressures were respectively 11 kPa and 4 MPa, and the total flow rate was 90 mL/min (NTP) with a catalyst weight of 15 mg. The catalyst thioresistance was evaluated by introducing an additional flow (10 mL/min) of a H_2S/H_2 mixture (Praxair, 500 ppm H_2S in H_2) to obtain 50 ppm of H_2S in the feed. Accordingly, in this case the tetralin partial pressure decreased to 10 kPa. The catalyst temperature was kept at 350 °C. Tetralin and reaction products (mainly *trans*/*cis* decalins, and traces of other C_{10} products; no C_{9-} products were detected) were analyzed online using a Hewlett Packard 6890 gas chromatograph equipped with a flame ionization detector and an Agilent HP1 column (25 m x 0.2 mm x 0.5 μm).

3. Results and discussion

3.1. TiO$_2$ rutile nanorods

Rutile titania nanorods synthesized hydrothermally from P25 titania (see Section 2.1) were used as a well-defined and strongly-interacting support for the metal nanoparticles.[37] An X-ray diffractogram of the nanorods is shown in Fig. S1 (ESI), revealing a pure rutile phase. Representative TEM images of the nanorods are reported in Figure 1a-b. They present an oblong shape (100-300 nm length) with square section (30-50 nm thickness, see inset in Fig. 1a). The nanorods are oriented along the [001] axis and selectively expose 80-90 % of (110) facets (Fig. 1d). The rod tips are formed mostly by (111) facets, but some rods have rounded terminations with no well-defined exposed plane (Fig. 1b). The specific surface area after heating at 350 °C in air is 30-35 m^2/g.

3.2. TiO$_2$-supported Au-Pd and Au-Rh catalyst characterization by (S)TEM

Au-Pd and Au-Rh nanoalloys, along with their monometallic counterparts, were synthesized by a colloidal method, followed by sol immobilization on the titania support (Section 2.1). The metal loadings of the prepared samples are reported in Table 1. Aberration-corrected TEM images of the fresh $Au_{54}Pd_{46}/TiO_2$ sample are shown in Figure 1c, while an aberration-corrected STEM-HAADF image of the fresh $Au_{63}Rh_{37}/TiO_2$ sample is shown in Figure 2a. In any case the catalysts exhibit a relatively sharp NP size distribution centered around 3 nm (Table 1 and Fig. 3), and the NPs are mostly faceted. However, as also observed by others,[10] the NPs are inhomogeneous in shape and atomic structure. Single-crystalline and twinned NPs are observed in each sample (see insets of Fig. 1c, and Fig. S2). Similar observations were made on unsupported AuRh@PVA colloids.[36] Moreover, the NPs exhibit weak epitaxy on the support, *i.e.* numerous epitaxial relationships could be observed.

Both for Au-Pd and Au-Rh samples, local EDX analyses reveal the bimetallic nature of the NPs. However, the chemical structure depends on the bimetallic system. In the case of Au-Pd, TEM (Fig. 1c-d) as well as STEM and XRD[36] suggest the formation of a solid solution with random distribution of Au and Pd atoms. Unlike for Au-Pd NPs synthesized by physical vapor deposition,[40] no long-range chemical order is detected within the chemically synthesized NPs. For Au-Rh, the characterization results rule out an extensive atomic-scale alloying of Au and Rh atoms. Instead, STEM-HAADF images of $Au_{63}Rh_{37}/TiO_2$ (see Fig. 2b) and unsupported AuRh@PVA colloids[36] exhibit signs of metal phase segregation within the NPs. The Au-rich areas appear brighter than the Rh-rich ones. HAADF-STEM was performed under favorable conditions of Z-contrast on Au-Rh due to the large difference in atomic numbers ($Z_{Au} = 79$, $Z_{Rh} = 45$, intensity $\sim Z^{1.7}$).[41]

The samples were exposed to oxidizing (air flow) and/or reducing (H_2 flow) thermal treatments in order to remove the PVA and thereby activate the catalysts. Low-temperature FTIR experiments in transmission mode performed on the $Au_{63}Rh_{37}/TiO_2$ sample show that both *in situ* reduction and calcination-reduction at 350 °C lead to surface dehydroxylation (Fig. 4a) and, most importantly, full removal of the adsorbed PVA (Fig. 4b). Indeed, the IR bands related to C-O and C-H vibrations in PVA[42] totally disappear upon treatments.

These treatments have no drastic influence on the NP size distributions, as shown by the size histograms of Figure 3. In the case of $Au_{46}Pd_{54}/TiO_2$, the smallest particles (< 2 nm) disappear upon treatments, and the size distributions become somewhat sharper and centered on 3.0 nm instead of 2.5 nm (Fig. 3a). For $Au_{63}Rh_{37}/TiO_2$, the size distribution shifts to slightly larger mean sizes (from 3.3 to 3.7 nm) upon reduction or becomes somewhat broader and bimodal on calcination-reduction. The size standard deviation increases from 1.0 to 1.3 nm (Fig. 3b).

TEM (Fig. 1d) and XRD[36] do not show any significant change of the Au-Pd NP structure upon treatment, the NPs retaining their alloyed configuration in all cases. Conversely, the reducing treatment leads to a structural modification of the Au-Rh NPs, as evidenced by STEM. Indeed, as in the example of Figure 2c, many of the NPs adopt a segregated "Janus-like" configuration, with $Au/Rh/TiO_2$ stacking. Note, however, that TEM and XRD[37] observations of amorphous "carbon black" powders highly loaded with AuRh NPs reveal partial intermixing between Au and Rh after reducing treatment. Finally, the calcination-reduction treatment (Fig. 2d) mostly leads to full metal segregation, with separated (smaller) Rh and (bigger) Au NPs, as determined from lattice parameter measurements on several images.

It is expected that oxidation-reduction at high temperature tends to fully separate metal phases, especially if the metals are poorly miscible in the bulk. The resulting oxides (or metal + oxide, as in the case of Au-Rh) have small affinity to each other, leading to phase segregation upon calcination.[43] The direct reducing treatment is less severe since the components of the nanoalloys remain in their metallic phase.

On the basis of the above results and the literature, it turns out that an intimate interaction, if possible, between Au and Rh atoms requires to finely tune the kinetics of Au and Rh salt reduction/nucleation. In any case, a thermal treatment restores the phase segregation driven by thermodynamics.

3.3. AuRh nanoparticle surface phase determination by CO-FTIR

The $Au_{63}Rh_{37}/TiO_2$ sample, either as-prepared or subjected to *in situ* pre-reduction/calcination-reduction at 350 °C, was characterized by FTIR spectroscopy after evacuating the cell and dosing a small amount of CO (which corresponds to saturation coverage on the metals) at LN_2 temperature. The results are presented in Figure 4c. The IR band assignments are based on published results for TiO_2,[44–47] Au,[45–47] and Rh[48–52] and by comparison to similar experiments performed on pure TiO_2, Au/TiO_2 and Rh/TiO_2 samples.[36]

The bands at 2180 cm^{-1} and 2157 cm^{-1} (both absent for the fresh sample) are related to CO chemisorbed on β'' Ti^{4+} Lewis acid sites and CO physisorbed on Ti-OH sites, respectively, while the bands at 2148 and 2138 cm^{-1} correspond to CO physisorption on TiO_2.[44–46]

While the fresh sample exhibits no metal-CO IR band, intense bands at 2104 cm^{-1} and 2071 cm^{-1}, corresponding to Au^0-CO (2105 cm^{-1} for Au/TiO_2) and Rh^0-CO (2069 cm^{-1} for Rh/TiO_2), respectively, are present for the calcined-reduced sample. This result is consistent with the above-mentioned STEM observations showing separated Au and Rh particles after calcination-reduction.

The reduced sample shows a broad band centered at 2067 cm^{-1} and a very small one near 2100 cm^{-1}, suggesting the quasi absence of gold at the surface. The comparison with STEM results further suggests that Janus-like NPs are surrounded by a thin Rh envelope. This hypothesis might seem contradictory with the above-mentioned lower surface energy of Au as compared to Rh, but it is in fact fully consistent with adsorption-induced surface segregation of the more reactive element.[2]

Additional CO-FTIR experiments on calcined Au(Rh)/TiO_2 samples show a distinct IR band centered at 2120 cm^{-1} only for Au/TiO_2 (Fig. S3). This band is assigned to cationic gold ($Au^{\delta+}$).[45] Hence, the presence of Rh may prevent Au from being: (i) oxidized on calcination and/or (ii) stabilized as $Au^{\delta+}$ in contact with TiO_2. This is consistent with a Rh shell (i) and/or the location of Rh at the interface between Au and TiO_2 demonstrated by STEM-HAADF images (ii).

3.4. Nanoalloy near-surface characterization by XPS

All the supported samples, either as-prepared or pre-oxidized/reduced at 350 °C, were analyzed by XPS. An unsupported AuRh@PVA sample was also analyzed for comparison. The spectra for Au 4f, Pd 3d and Rh 3d core levels are shown in Figure 5.

The presence of TiO_2 induces a downshift in the binding energy of the Au 4f and Rh 3d core levels, with respect to AuRh@PVA. For the latter, the Au $4f^{7/2}$ (84.1 eV) and Rh $3d^{5/2}$ (307.2 eV) peak positions agree well with bulk Au^0 (83.95 eV) and Rh^0 (307.2 eV) reference values,[53] respectively. The downshift by 0.4-0.7 eV observed for TiO_2-supported samples can be ascribed to electron transfer from titania to the metal.[54]

The $AuPd/TiO_2$ samples show downshifts of Au 4f (0.4 eV) and Pd 3d (0.3-0.8 eV) core levels as compared to the Au/TiO_2 and Pd/TiO_2 cases. This is consistent with the Au-Pd atomic-scale alloying mentioned above.[11] It was previously explained by a charge compensation model in which Pd donates *sp* electrons to Au while Au donates *d* electrons to Pd.[55] The $AuRh/TiO_2$ samples exhibit only slight downshifts of the Au 4f (<0.3 eV) and Rh 3d (<0.2 eV) core levels with respect to their Au/TiO_2 and Rh/TiO_2 counterparts, consistent with the limited extent of Au-Rh atomic-scale alloying mentioned previously.

With respect to pre-reduced Pd/TiO_2 and $AuPd/TiO_2$ samples showing only a Pd^0 contribution at the Pd $3d^{3/2}$ core level, the fresh samples exhibit an additional contribution (denoted Pd^{m+} in Fig. 5a, $m \approx$ 2) at higher binding energy, which corresponds to oxidized Pd.[17] Note that the Pd $3d^{5/2}$ core level is close to the Au $4d^{5/2}$ one, which prevents us from using the 5/2 levels for comparison between AuPd and Pd. Interestingly, the fraction of Pd^{m+} is much smaller in the case of AuPd, suggesting a stabilizing effect of Au on Pd oxidation in air. A similar effect is shown in Figure 5b for Rh and AuRh samples: the latter exhibit proportionally smaller Rh oxide contributions (two $Rh^{\delta+}$ and Rh^{n+} oxidation states are present, with $\delta < n$, n = 3 or 4)[23,27,53] than the Rh samples. These contributions are well observed on the pre-calcined sample, while they are absent for the reduced samples. Furthermore, comparing the Rh 3d signals for fresh AuRh@PVA and $AuRh/TiO_2$ samples in Figure 5b, it is seen that the Rh oxide fractions are much larger in the former case (with $[Rh^{n+}] > [Rh^{\delta+}]$). This also suggests an inhibiting effect of the titania support on Rh oxidation or a partial reduction of Rh oxides upon NP deposition on titania.

Finally, the quantification shows that Au/Pd and Au/Rh ratios agree with the those determined by elemental analysis within 6 % (Fig. 5). The only exception is the calcined Au-Rh sample which exhibits an enrichment in Rh, suggesting a possible core-shell $Au@RhO_x$ restructuring. However, it should be noticed that the electron mean free path being of 1.7 nm for Au, 1.9 nm for Rh, and 2.5 nm for Pd at the X-ray primary energy of 1486.6 eV,[56] and the NP dimension being of *ca.* 3 nm, both the bulk and the surface of the NPs are probed by XPS.

3.5. Evaluation of the catalysts for tetralin hydrogenation in the presence of H_2S

The catalytic tests were performed in the gas phase using a flow fixed bed reactor at high H_2 pressure (4 MPa) and 350 °C. The tests were preceded by *in situ* pretreatment of the fresh samples under pure hydrogen flow at 4 MPa for 3 h at 350 °C. *Trans*-decalin and *cis*-decalin are the only reaction products, *i.e.*, tetralin is fully hydrogenated in these conditions. Figure 6a shows the evolution of

tetralin conversion with time-on-stream on the titania-supported catalysts. Note that Au/TiO_2 exhibited negligible activity (not shown here). The initial gradual decrease of the conversion is due to slow poisoning of the metal surface by sulfur impurities present in the reactor, even before addition of H_2S to the reaction feed. However, this decrease is slower on Rh-based catalysts than on Pd-based ones. Furthermore, with respect to Rh/TiO_2, the deactivation rate is smaller for $Au_{36}Rh_{64}/TiO_2$, and negligible for $Au_{57}Rh_{43}/TiO_2$, suggesting a stabilizing effect of Au on Rh.

Upon addition of H_2S, Pd/TiO_2 immediately loses part of its activity, then gradually deactivates. Going back to S-free conditions, the catalyst somewhat regenerates and stabilizes. $AuPd/TiO_2$ shows a different behavior since H_2S has initially a beneficial effect on the activity. We ascribe these results to the sulfidation of Pd in contact with H_2S. In our conditions, the Pd_4S phase, which is known to possess poor aromatics hydrogenation efficiency,[14] is most likely formed.[57] Alloying with Au seems to prevent Pd sulfidation, in agreement with previous works.[13,14]

Rh/TiO_2 has a radically different behavior as compared to Pd-based catalysts: the addition of H_2S is seen to continuously activate the catalyst, suggesting a highly active Rh sulfide phase. The gradual decrease of the conversion without H_2S in the feed could be the result of slow poisoning of the metal surface by strong adsorption of the reactants, the reaction products, or H_2S. Most probably, the role of sulfur impurities, causing the formation of a less sulfided Rh surface phase with poor activity, cannot be ruled out. In contrast, for the two $Au-Rh/TiO_2$ catalysts, H_2S has a limited influence on the conversion rate, and the activity only slightly decreases over 35 h of reaction. Hence, the addition of Au limits the influence of H_2S on Rh, as for the case of Pd.

Figure 6b summarizes the results for the Rh-based catalysts in terms of *trans*/*cis* decalin selectivity and activity per Rh weight at quasi steady state. The *trans*/*cis* ratio, comprised between 1.7 and 3.8, is much lower than its value at thermodynamic equilibrium in our pressure and temperature conditions (6.7). The tetralin hydrogenation activity strongly decreases as the gold concentration increases, similarly to the findings of García *et al.* for cyclohexene hydrogenation,[34] suggesting that Au partially blocks hydrogenation sites.

4. Conclusion

The XPS and catalysis results point to a stabilizing effect of gold on the surface oxidation and sulfidation resistance of the Pt-group metals, respectively. In the case of Au-Pd nanoalloys, which exhibit solid-solution structure, this phenomenon can be confidently ascribed to the atomic-scale interaction between the two metals through electronic effects. In particular, the H_2S dissociation barrier is much higher and the sulfur adsorption energy much lower on Au than on the Pt-group metals.[58] The case of Au-Rh is more intriguing since STEM observations evidence at least partially segregated phases for the as-prepared catalysts and an $Au/Rh/TiO_2$ stacked segregated structure for the pre-reduced ones. However, the somewhat detrimental effect of gold on tetralin hydrogenation activity shows that the catalyst may retain the latter structure under severe reducing reaction conditions, a thick gold layer protecting in part the Rh phase from sulfidation by H_2S. Further investigations of the $Au-Rh/TiO_2$ system are currently undertaken to rationalize the observed structures and the gold stabilizing effect.

References

1   R. Ferrando, J. Jellinek and R. L. Johnston, *Chem. Rev.*, 2008, **108**, 845–910.
2   L. Piccolo, in *Nanoalloys: Synthesis, Structure and Properties*, Springer-Verlag, London, D. Alloyeau, C. Mottet, C. Ricolleau (Eds.)., 2012.
3   A. Stanislaus and B. H. Cooper, *Catal. Rev. Sci. Eng.*, 1994, **36**, 75–123.
4   C. H. Bartholomew, P. K. Agrawal and J. R. Katzer, *Adv. Catal.*, 1982, **31**, 135–242.
5   S. Nassreddine, L. Massin, M. Aouine, C. Geantet and L. Piccolo, *J. Catal.*, 2011, **278**, 253–265.
6   N. Toshima, M. Harada, Y. Yamazaki and K. Asakura, *J. Phys. Chem.*, 1992, **96**, 9927–9933.
7   N. Toshima, *Pure Appl. Chem.*, 2000, **72**, 317–325.
8   N. Dimitratos, F. Porta and L. Prati, *Appl. Catal. Gen.*, 2005, **291**, 210–214.
9   N. Dimitratos, J. A. Lopez-Sanchez, D. Morgan, A. F. Carley, R. Tiruvalam, C. J. Kiely, D. Bethell and G. J. Hutchings, *Phys. Chem. Chem. Phys.*, 2009, **11**, 5142–5153.
10 G. J. Hutchings and C. J. Kiely, *Acc. Chem. Res.*, 2013, **46**, 1759–1772.
11 C.-W. Yi, K. Luo, T. Wei and D. W. Goodman, *J. Phys. Chem. B*, 2005, **109**, 18535–18540.
12 F. Gao and D. W. Goodman, *Chem. Soc. Rev.*, 2012, **41**, 8009–8020.
13 A. M. Venezia, V. La Parola, V. Nicolì and G. Deganello, *J. Catal.*, 2002, **212**, 56–62.
14 B. Pawelec, A. M. Venezia, V. La Parola, E. Cano-Serrano, J. M. Campos-Martin and J. L. G. Fierro, *Appl. Surf. Sci.*, 2005, **242**, 380–391.
15 L. Piccolo, A. Piednoir and J.-C. Bertolini, *Surf. Sci.*, 2005, **592**, 169–181.
16 A. Hugon, L. Delannoy, J.-M. Krafft and C. Louis, *J. Phys. Chem. C*, 2010, **114**, 10823–10835.
17 Z. Zhang, S.-W. Cao, Y. Liao and C. Xue, *Appl. Catal. B Environ.*, 2015, **162**, 204–209.
18 H. Okamoto and T. B. Massalski, *Bull. Alloy Phase Diagr.*, 1985, **6**, 229–235.
19 F. R. de Boer, R. Boom, W. C. M. Mattens, A. R. Miedema and A. K. Niessen, *Cohesion in Metals: Transition Metal Alloys*, North-Holland Physics Publishing, 1989.
20 L. Vitos, A. V. Ruban, H. L. Skriver and J. Kollár, *Surf. Sci.*, 1998, **411**, 186–202.
21 J. Creuze, I. Braems, F. Berthier, C. Mottet, G. Tréglia and B. Legrand, *Phys. Rev. B*, 2008, **78**, 075413.
22 H. Okamoto and T. B. Massalski, *Bull. Alloy Phase Diagr.*, 1984, **5**, 384–387.
23 J. Raskó, Á. Koós, K. Baán and J. Kiss, *React. Kinet. Catal. Lett.*, 2007, **90**, 187–195.
24 L. Óvári, L. Bugyi, Z. Majzik, A. Berkó and J. Kiss, *J. Phys. Chem. C*, 2008, **112**, 18011–18016.
25 L. Óvári, A. Berkó, N. Balázs, Z. Majzik and J. Kiss, *Langmuir*, 2009, **26**, 2167–2175.
26 A. Kukovecz, G. Potari, A. Oszko, Z. Konya, A. Erdohelyi and J. Kiss, *Surf. Sci.*, 2011, **605**, 1048–1055.

27 J. Kiss, L. Óvári, A. Oszkó, G. Pótári, M. Tóth, K. Baán and A. Erdóhelyi, *Catal. Today*, 2012, **181**, 163–170.

28 L. Óvári, A. Berkó, R. Gubó, Á. Rácz and Z. Kónya, *J. Phys. Chem. C*, 2014, **118**, 12340–12352.

29 R. L. Chantry, W. Siriwatcharapiboon, S. L. Horswell, A. J. Logsdail, R. L. Johnston and Z. Y. Li, *J. Phys. Chem. C*, 2012, **116**, 10312–10317.

30 R. L. Chantry, I. Atanasov, W. Siriwatcharapiboon, B. P. Khanal, E. R. Zubarev, S. L. Horswell, R. L. Johnston and Z. Y. Li, *Nanoscale*, 2013, **5**, 7452–7457.

31 R. L. Chantry, I. Atanasov, S. L. Horswell, Z. Y. Li and R. L. Johnston, in *Gold Clusters, Colloids and Nanoparticles II*, ed. D. M. P. Mingos, Springer International Publishing, 2014, pp. 67–90.

32 E. R. Essinger-Hileman, D. DeCicco, J. F. Bondi and R. E. Schaak, *J Mater Chem*, 2011, **21**, 11599–11604.

33 S. García, R. M. Anderson, H. Celio, N. Dahal, A. Dolocan, J. Zhou and S. M. Humphrey, *Chem. Commun.*, 2013, **49**, 4241–4243.

34 S. García, L. Zhang, G. W. Piburn, G. Henkelman and S. M. Humphrey, *ACS Nano*, 2014, **8**, 11512–11521.

35 H. Li and P. Afanasiev, *Mater. Res. Bull.*, 2011, **46**, 2506–2514.

36 L. Piccolo et al., to be published.

37 Z. Konuspayeva, G. Berhault, P. Afanasiev, T.-S. Nguyen, A. Auyezov, M. Burkitbayev and L. Piccolo, in *MRS Proceedings*, MRS Online Proceedings Library, 2014, vol. 1641, pp. mrsf13–1641–aa08–07.

38 Z. Konuspayeva, PhD thesis, Université Claude Bernard - Lyon 1, 2014.

39 C. Ricolleau, J. Nelayah, T. Oikawa, Y. Kohno, N. Braidy, G. Wang, F. Hue, L. Florea, V. P. Bohnes and D. Alloyeau, *Microscopy*, 2013, **62**, 283–293.

40 J. Nelayah, N. T. Nguyen, D. Alloyeau, G. Y. Wang and C. Ricolleau, *Nanoscale*, 2014, **6**, 10423.

41 Z. Y. Li, in *Frontiers of Nanoscience*, eds. J. P. Wilcoxon and R. L. Johnston, Elsevier, 2012, vol. 3, pp. 213–247.

42 T. Nedoseykina, P. Plyusnin, Y. Shubin and S. Korenev, *J. Therm. Anal. Calorim.*, 2010, **102**, 703–708.

43 S. Zhou, H. Yin, V. Schwartz, Z. Wu, D. Mullins, B. Eichhorn, S. H. Overbury and S. Dai, *ChemPhysChem*, 2008, **9**, 2475–2479.

44 K. Hadjiivanov, *Appl. Surf. Sci.*, 1998, **135**, 331–338.

45 F. Boccuzzi and A. Chiorino, *J. Phys. Chem. B*, 2000, **104**, 5414–5416.

46 H. Klimev, K. Fajerwerg, K. Chakarova, L. Delannoy, C. Louis and K. Hadjiivanov, *J. Mater. Sci.*, 2007, **42**, 3299–3306.

47 L. Piccolo, H. Daly, A. Valcarcel and F. C. Meunier, *Appl. Catal. B Environ.*, 2009, **86**, 190–195.

48 M. Primet, *J. Chem. Soc. Faraday Trans. 1 Phys. Chem. Condens. Phases*, 1978, **74**, 2570–2580.

49 J. T. Yates, T. M. Duncan, S. D. Worley and R. W. Vaughan, *J. Chem. Phys.*, 1979, **70**, 1219–1224.

50 F. Solymosi and M. Pasztor, *J. Phys. Chem.*, 1985, **89**, 4789–4793.

51 L. L. Sheu and W. M. H. Sachtler, *J. Mol. Catal.*, 1993, **81**, 267–278.

52 S. Trautmann and M. Baerns, *J. Catal.*, 1994, **150**, 335–344.

53 *NIST X-ray Photoelectron Spectroscopy Database, Version 4.1, http://srdata.nist.gov/xps/*, National Institute of Standards and Technology, Gaithersburg, 2012.

54 A. Zwijnenburg, A. Goossens, W. G. Sloof, M. W. J. Crajé, A. M. van der Kraan, L. Jos de Jongh, M. Makkee and J. A. Moulijn, *J. Phys. Chem. B*, 2002, **106**, 9853–9862.

55 Y. S. Lee, Y. Jeon, Y. D. Chung, K. Y. Lim, C. N. Whang and S. J. Oh, *J. Korean Phys. Soc.*, 2000, **37**, 451–455.

56 C. J. Powell and A. Jablonski, *NIST Electron Inelastic-Mean-Free-Path Database, Version 1.2, SRD 71*, National Insititute of Standards and Technology, Gaithersburg, MD, 2010.

57 E. J. M. Hensen, H. J. A. Brans, G. M. H. J. Lardinois, V. H. J. de Beer, J. A. R. van Veen and R. A. van Santen, *J. Catal.*, 2000, **192**, 98–107.

58 D. R. Alfonso, *Surf. Sci.*, 2008, **602**, 2758–2768.

Table 1. Metal content (ICP-OES) and metal particle size (TEM) of the as-prepared catalysts.

Metal compos. (at%)	Metal loading (wt%)	NP size (nm)
Au	1.5	2.8 ± 0.8
Au	1.8	-
Pd	0.82	1.7 ± 0.7
Rh	0.64	-
Rh	0.62	2.4 ± 0.6
$Au_{46}Pd_{54}$	2.4	2.5 ± 1.0
$Au_{37}Rh_{63}$	2.4	3.2 ± 1.2
$Au_{55}Rh_{45}$	2.3	3.3 ± 1.0
$Au_{57}Rh_{43}$	2.2	4.0 ± 1.3
$Au_{63}Rh_{37}$	2.5	3.3 ± 1.0

Fig 1. Representative aberration-corrected TEM images of TiO$_2$ (a, b) and Au$_{46}$Pd$_{54}$/TiO$_2$ (c: fresh; d: reduced). Inset of (a): cross-sectional view of a nanorod. Insets of (c): HRTEM images of three nanoparticles (the facets are indexed in Fig. S2). Inset of (d): FFT of an NP-free TiO$_2$ zone.
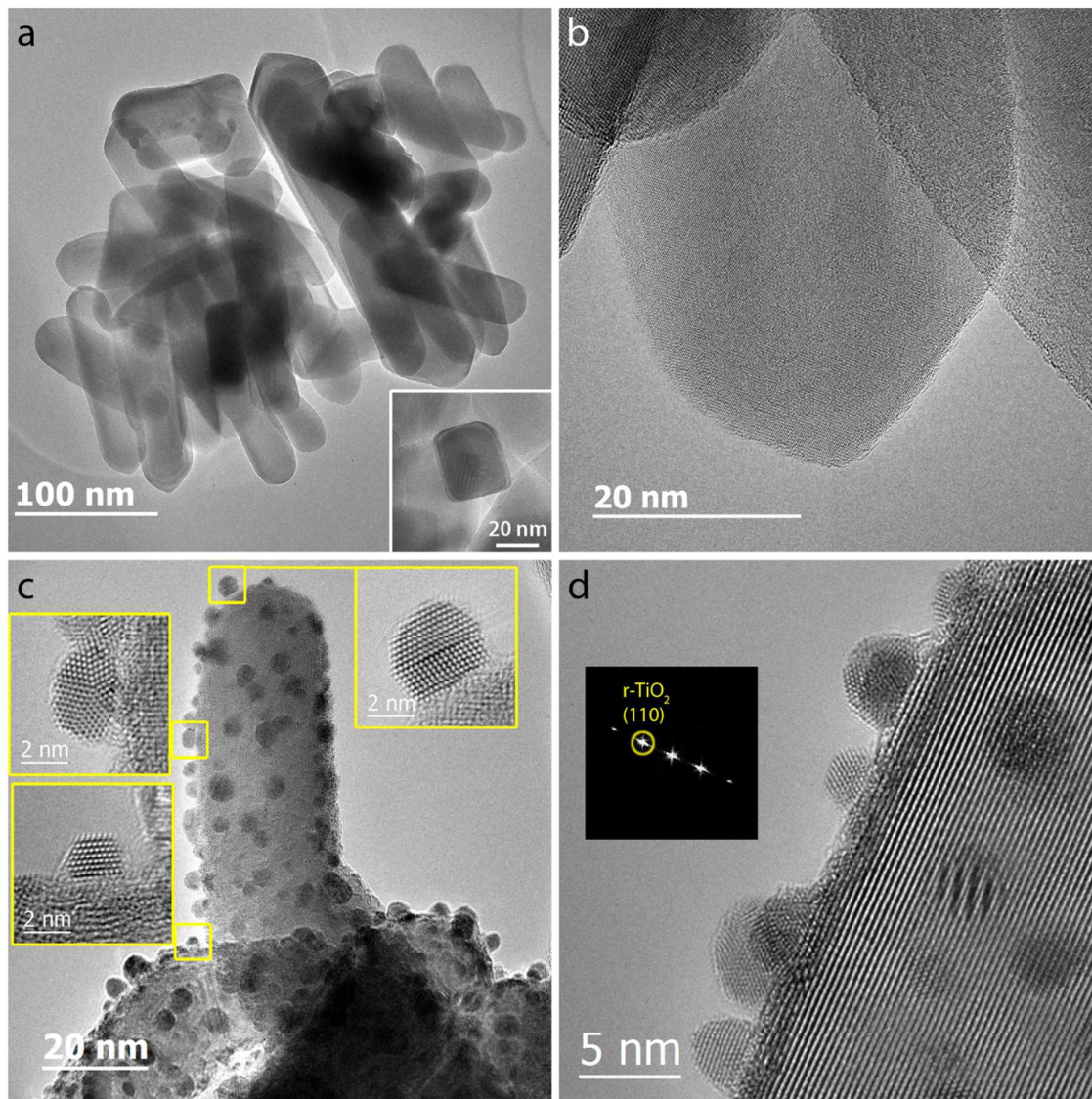
Fig 2. Representative aberration-corrected STEM-HAADF images of $Au_{63}Rh_{37}/TiO_2$: (a, b) fresh sample; (c) reduced sample; (d) calcined-reduced sample. The arrows in (b) indicate signs of metal segregation.
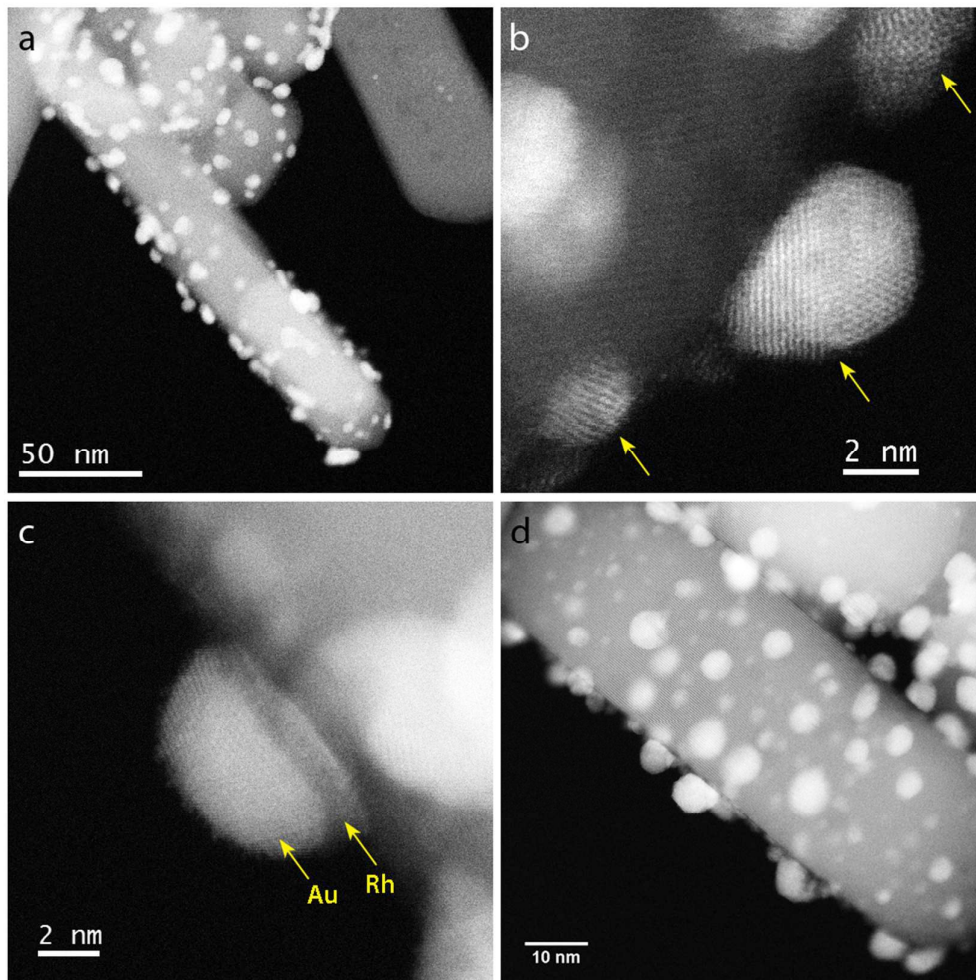
Fig 3. NP size distributions determined from (S)TEM for fresh, reduced, and calcined-reduced $Au_{46}Pd_{54}/TiO_2$ (a) and $Au_{63}Rh_{37}/TiO_2$ (b). The average size and standard deviation are indicated.
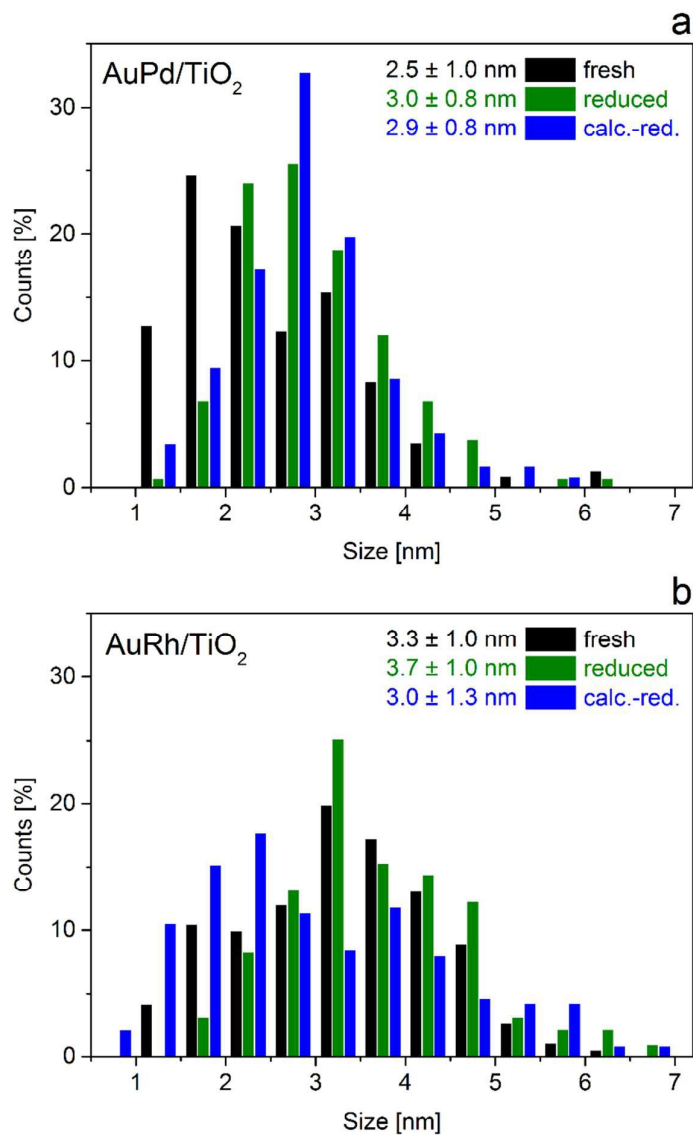
Fig 4. FTIR spectra recorded at -196 °C for $Au_{63}Rh_{37}/TiO_2$ after introduction of 4.2 µmol CO: (a) Hydroxyl region; (b) PVA region; (c) Carbonyl region. The treatments at 350 °C were applied *in situ*.

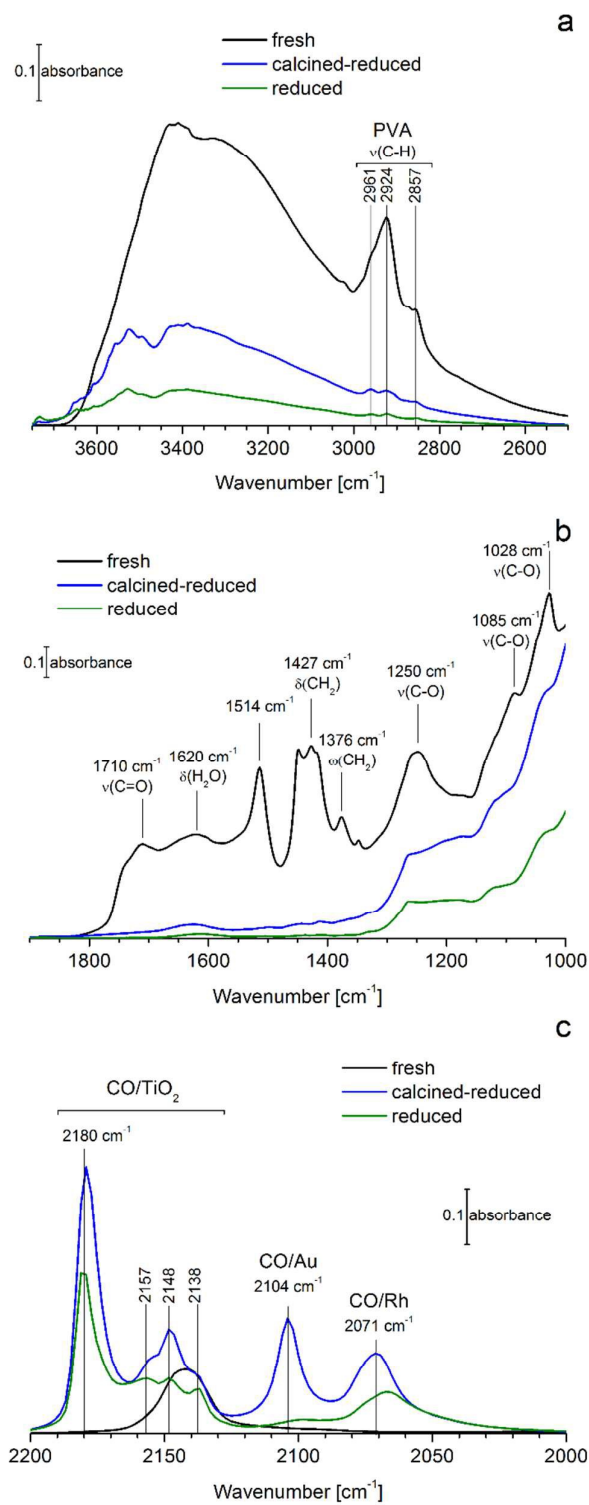**Fig. 5.** XPS spectra for AuRh@PVA (fresh) and TiO$_2$-supported Au, Pd, Rh, Au$_{46}$Pd$_{54}$, Au$_{37}$Rh$_{63}$, Au$_{57}$Rh$_{43}$, and Au$_{63}$Rh$_{37}$ catalysts (fresh, calcined, or reduced): (a) Au, Pd and Au-Pd samples; (b) Au, Rh and Au-Rh samples. The hatched rectangles indicate the ranges of peak positions. Each spectrum was normalized by the total area of metal contributions. The numbers at the right-hand side give the Au concentrations (at%) determined by XPS. The values between brackets are the Au concentrations determined by elemental analysis of the samples.
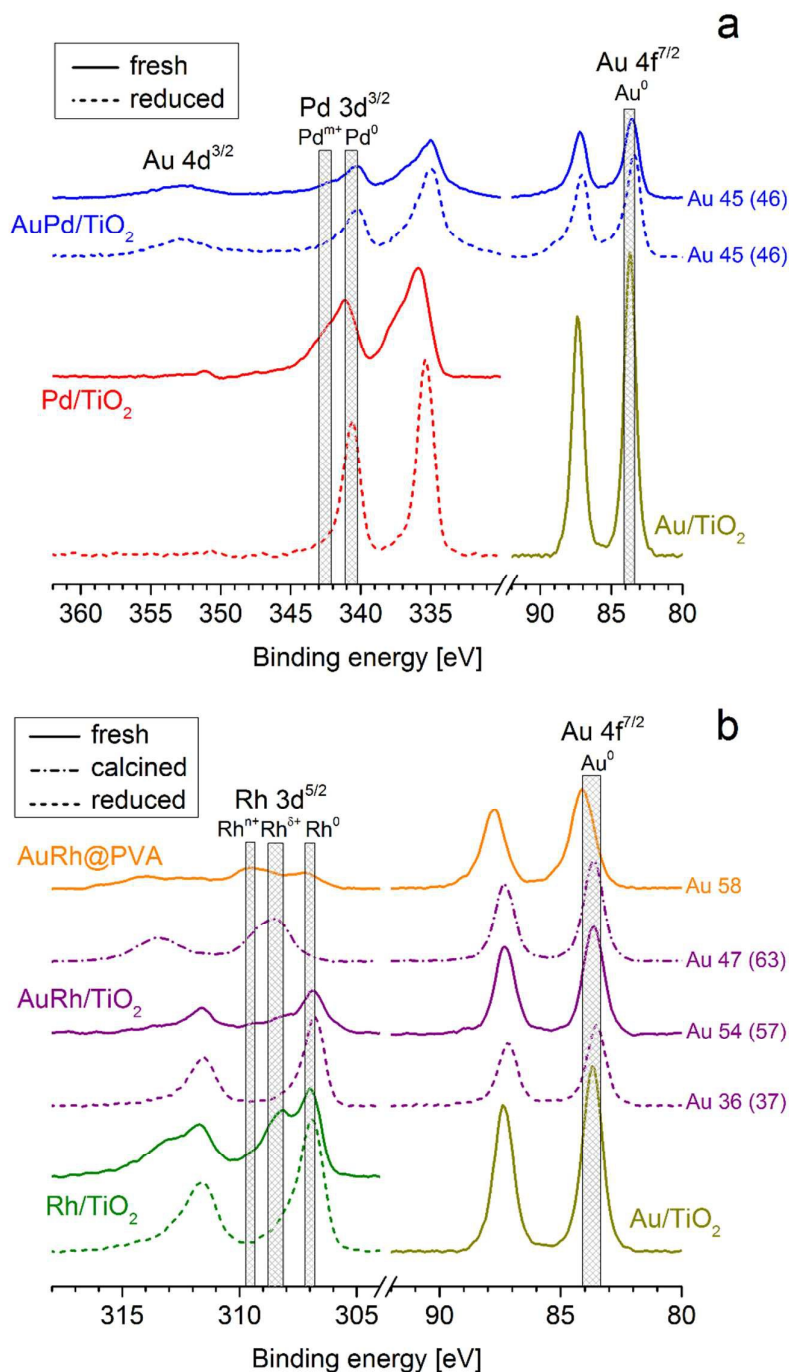
Fig. 6. (a) Tetralin conversion *versus* time on all the TiO$_2$-supported catalysts without and with 50 ppm H$_2$S in the tetralin-hydrogen feed. (b) Tetralin conversion activity (blue square dots, right Y axis) and selectivity to *cis-* and *trans-* decalins (grey bars, left Y axis) of (Au-)Rh/TiO$_2$ catalysts at quasi steady state.